Coupled Aero-Hydro-Servo-Elastic Methods for Floating Wind Turbines

Jiahao Chen[a,c], Zhiqiang Hu[b,*], Geliang Liu[a], Decheng Wan[a,c]

[a]State Key Laboratory of Ocean Engineering, Shanghai Jiao Tong University, Shanghai, China

[b]School of Engineering, Newcastle University, Newcastle upon Tyne, UK

[c]Collaborative Innovation Center for Advanced Ship and Deep-Sea Exploration, Shanghai Jiao Tong University, Shanghai, China

* Corresponding author:

E-mail: Zhiqiang.Hu@newcastle.ac.uk (Zhiqiang Hu)

School of Engineering, Newcastle University, Newcastle upon Tyne, UK

NE1 7RU, Newcastle upon Tyne, UK

ABSTRACT

To meet the demand of the development of floating wind turbines, coupled aero-hydro-servo-elastic methods were developed and then were programmed as an integrated code DARwind (short for Dynamic Analysis for Response of Wind Turbines) for simulating floating wind turbines. This paper first presents the theoretical background, including Kane's dynamical equations in combination with the Cardan angles method, the hybrid coordinate dynamic analysis method, and the adjacent array approach for kinematics and kinetics. The blade element/momentum method with aerodynamic corrections was used for aerodynamic simulation. Potential-flow theory, the second-order wave forces and the Morison formula with the strip theory were used for hydrodynamics, and a quasi-static mooring modelling approach was developed for the catenary mooring system. A generator-torque controller and a full-span rotor-collective blade-pitch controller were adopted for control strategies. The code was then verified by a series of code-to-experiment comparisons, including the mooring system, the structural elasticity, the aerodynamic performance, the hydrodynamic performance and the control strategy. The comparisons demonstrated that the coupled aero-hydro-servo-elastic methods have a satisfactory ability to perform fully coupled simulations for floating wind turbines.

Keywords: floating offshore wind turbines; DARwind; Kane's dynamical equations; aerodynamics; hydrodynamics; code-to-experiment validation;

1. Introduction

In recent years, the rapid development of the offshore wind industry has been attracting increasing worldwide attention [1]. Currently, offshore wind turbines can be classified into two categories [2]: bottom-mounted offshore wind turbines and floating offshore wind turbines (FOWTs). Compared with the bottom-mounted turbines, which are limited to water depths of 30 m, FOWTs can take advantage of abundant wind resources in deeper water regions [3].

To demonstrate the technical feasibility of the proposed FOWTs, three methods are generally applied, including onsite measurements, scaled model tests and numerical analysis. The first full-scale FOWT demonstration of the onsite measurement method was conducted off the coast of Norway in 2009 using the Hywind turbine (a spar-type FOWT) [4]. In 2011, a semi-submersible FOWT, WindFloat, was deployed 5 km off Portugal's coast [5]. From 2013 to 2015, the Fukushima floating offshore wind farm

demonstration project was conducted with three different FOWTs and one floating power sub-station [6]. The first offshore grid-connected wind turbine in the Americas, VolturnUS, was tested for 18 months from 2013 to 2014 off Castine in eastern Maine, USA [7]. With respect to scaled model tests, the Hydro Oil & Energy Company supported a $1/47^{th}$ scale 5-MW spar-type FOWT model test at the MARINTEK (Norwegian Marine Technology Research Institute) in 2006 [8]. In 2012, $1/50^{th}$ scale model tests were conducted at the Maritime Research Institute Netherlands (MARIN) with a tension-leg FOWT, a spar-type FOWT, and a semi-submersible FOWT [9]. The public details of the MARIN's experiments greatly promoted the worldwide development of the FOWT model tests. In 2013, a $1/50^{th}$ scale model test using a spar-type FOWT and a semi-submersible FOWT was conducted at the Deepwater Offshore Basin of Shanghai Jiao Tong University [10, 11]. In 2014, a $1/50^{th}$ scale combined wind and wave power generation system model, STC, was conducted at the towing tank of the MARINTEK [12]. However, onsite measurements and scaled model tests have generally required great amounts of money and time. Moreover, most of these experimental projects relied quite heavily on industrial investments, which make the valuable measured data unavailable to normal researchers. In contrast, the numerical analysis method for FOWTs is cheaper, faster and more convenient. Therefore, more and more efforts are being devoted to the development of reliable numerical tools for FOWTs. Currently, there are two popular numerical analysis methods for FOWTs: the frequency-domain analysis method and the time-domain analysis method [13].

Learning from the technologies of offshore O&G industries in the field, some researchers have studied the dynamical characteristics of FOWTs using frequency-domain analysis tools. For example, Lee *et al.* [14] carried out preliminary investigations on a TLP FOWT by the linear frequency-domain analysis method. Wayman *et al.* [15] analysed the shallow-drafted barge FOWT and the MIT/NREL TLP FOWT using frequency-domain analysis technology. However, there are some limitations in the frequency-domain analysis method. For example, it is not capable of modelling non-linear dynamic behaviours, transient events and controllers, which are generally important for FOWTs.

By comparison, the time-domain analysis method is more appropriate for FOWTs. In the time-domain analysis, a FOWT can be considered as a fully coupled aero-hydro-servo-elastic model by solving the dynamical equations of numerous degrees of freedom. For instance, Madjid *et al.* [16] studied extreme structural response and fatigue loads of a spar-type FOWT in the time-domain. Bachynski *et al.* [17] conducted investigation on transient events for FOWTs, e.g., pitch actuator fault, grid loss, and shutdown in the time-domain. More and more efforts are devoted to the development of time-domain analysis tools currently.

Nonetheless, fully coupled time-domain numerical tools for FOWTs remain limited. Some are developed from the commercially available general-purpose multibody-system (MBS, for short) codes combined with aerodynamic, mooring and hydrodynamic subroutines. For example, Withee *et al.* [18] conducted research on FOWTs using ADAMS (a commercial general-purpose MBS code for the aerospace and robotics industries) in combination with additional aerodynamic and hydrodynamic subroutines. Similarly, Matha *et al.* [19] made use of another commercial general-purpose MBS code, SIMPACK, with an aerodynamic subroutine package AeroDyn, a hydrodynamic subroutine package HydroDyn, and a developed mooring-lines subroutine. On the other hand, some time-domain numerical tools are developed from codes originally for onshore bottom-mounted wind turbines; for example, Jonkman [20, 21] recoded the land-based horizontal-axis wind turbine simulation code FAST and developed its capacity for calculating hydrodynamic loads and mooring loads on FOWTs. Some time-domain simulation tools have been developed from the field of offshore structures in the O&G

industries; for instance, Fylling *et al.* [22] conducted research on FOWTs using SIMO/RIFLEX combined with a separate aerodynamic subroutine; SIMO is used to simulate structural dynamics and hydrodynamics, and RIFLEX is used to model mooring lines with FEM technology. In recent years, some researchers have attempted to make use of computational fluid dynamics (CFD) tools to model FOWTs. Wan *et al.* [23, 24] conducted a series of investigations on dynamical characteristics of FOWTs using their CFD tool NAOE-FOAM-SJTU. Nematbakhsh *et al.* [25] conducted a series of comparisons of wave load effects on a TLP FOWT using CFD and potential flow theory approaches. Up to now, the development of adequate fully coupled time-domain FOWT simulation tools is in progress, and is still important for the research of FOWTs.

The Offshore Code Comparison Collaboration (OC3) project [26] and the Offshore Code Comparison Collaboration Continuation (OC4) project [27] performed a successive series of code-to-code comparisons to verify the technical feasibility of the FOWTs numerical tools. Nonetheless, detailed code-to-experiment comparisons are still relatively few because of the scarcity of the FOWT test data being openly available to the public.

In view of the above-mentioned facts, an integrated code DARwind (short for Dynamic Analysis for Response of Wind Turbines) based on fully coupled aero-hydro-servo-elastic methods was developed for simulating FOWTs in this paper. For kinematics and kinetics, Kane's dynamical method [28] in combination with the Cardan angles method [29], the hybrid coordinate dynamical method [30], the nonlinear deformations model and the adjacent array approach [31] were applied to establish the fully coupled multi-body dynamic model for FOWTs. For aerodynamics, the blade element/momentum method [32] with aerodynamic corrections [33] was used to calculate aerodynamic loads. For hydrodynamics [34], the linear potential-flow theory, the second-order wave forces theory and the Morison formula with the strip theory were applied to account for hydrodynamic loads. For mooring systems, a quasi-static approach [35] for taut or slack catenary lines considering stretching was developed. For control strategies [36], a combination of a generator-torque controller and a full-span rotor-collective blade-pitch controller was implemented. The paper detailed outline of the utilized coupled aero-hydro-servo-elastic methods and then conducted a series of verifications by means of experimental results. It benefits our understanding of the coupled dynamical theories on FOWTs and facilitates the development of additional FOWTs numerical codes.

This paper is organized as follows: In Section 2, theories regarding the kinematics and kinetics, aerodynamics, hydrodynamics, mooring system modelling, and control strategies in the code are presented, respectively. In Section 3, a brief description of the model and the experiment is presented. Finally, verifications of the accuracy of the code, by means of a series of code-to-experiment comparisons, are presented in Section 4.

2. Theoretical background

2.1. Kinematics and kinetics

The kinematics and kinetics are vital for a FOWT system, thus the relevant theories are introduced in this subsection as follows: the method for rotational and translational motions of a body is presented first. Then, a description of the topological configuration, coordinate systems, and degrees of freedom is given. Finally, the establishment of the system's dynamical governing equations using Kane's dynamical method is detailed.

According to Euler's theorem on rotations [37], a limited rotation of a body about one point can be

decomposed as three limited angles corresponding three different coordinate axes. The Cardan angles method [29] is used to describe these angles because it is simple and suitable in the case of small angular motion of a FOWT. As shown in **Fig. 1**, we assume that the rotational motion of a body about a point in a Cartesian coordinate system can be decomposed into the following steps (a 1-2-3 Euler rotation sequence): (1) the frame $\boldsymbol{e}^{(0)}$ moves to $\boldsymbol{e}^{(1)}$ by rotating about $\boldsymbol{e}_1^{(0)}$ at the degree of α; (2) the frame $\boldsymbol{e}^{(1)}$ then rotates about $\boldsymbol{e}_2^{(1)}$ at the degree of β to the frame $\boldsymbol{e}^{(2)}$; (3) finally, the frame $\boldsymbol{e}^{(2)}$ moves to its actual position $\boldsymbol{e}^{(3)}$ by rotating about $\boldsymbol{e}_3^{(2)}$ at the degree of γ. In this process, α, β and γ are the so-called "Cardan angles".

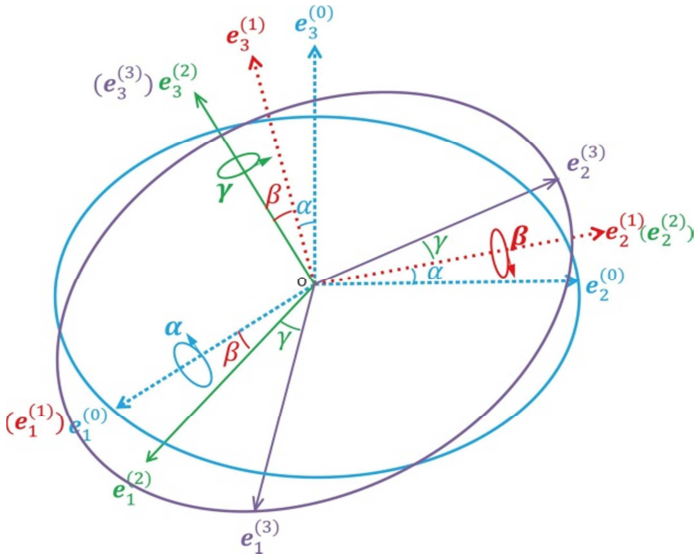

Fig. 1. Cardan angles.

Based on the Cardan angles method, the direction cosine matrix between frames can be written as:

$$\boldsymbol{T^{03}} = \begin{bmatrix} cos\beta cos\gamma & -cos\beta sin\gamma & sin\beta \\ sin\alpha sin\beta cos\gamma + cos\alpha sin\gamma & -sin\alpha sin\beta sin\gamma + cos\alpha cos\gamma & -sin\alpha cos\beta \\ -cos\alpha sin\beta cos\gamma + sin\alpha sin\gamma & cos\alpha sin\beta sin\gamma + sin\alpha cos\gamma & cos\alpha cos\beta \end{bmatrix} \tag{1}$$

It is convenient to transform coordinates between different frames using the above direction cosine matrix. For example, the transformation between the frame $\boldsymbol{e}^{(3)}$ and $\boldsymbol{e}^{(0)}$ can be given by:

$$\begin{bmatrix} x_0 \\ y_0 \\ z_0 \end{bmatrix}_{\boldsymbol{e}^{(0)}} = \boldsymbol{T^{03}} \cdot \begin{bmatrix} x \\ y \\ z \end{bmatrix}_{\boldsymbol{e}^{(3)}} \tag{2}$$

or

$$\begin{bmatrix} x \\ y \\ z \end{bmatrix}_{\boldsymbol{e}^{(3)}} = (\boldsymbol{T^{03}})^{-1} \cdot \begin{bmatrix} x_0 \\ y_0 \\ z_0 \end{bmatrix}_{\boldsymbol{e}^{(0)}} \tag{3}$$

Using the Cardan angles method, the angular velocity and acceleration of a body with respect to its body-fixed frame $\boldsymbol{e}^{(3)}$ can be written as follows:

$$\boldsymbol{\omega} = \dot{\alpha}\boldsymbol{e}_1^{(0)} + \dot{\beta}\boldsymbol{e}_2^{(1)} + \dot{\gamma}\boldsymbol{e}_3^{(2)} = \begin{bmatrix} cos\beta cos\gamma & sin\gamma & 0 \\ -cos\beta sin\gamma & cos\gamma & 0 \\ sin\beta & 0 & 1 \end{bmatrix} \begin{bmatrix} \dot{\alpha} \\ \dot{\beta} \\ \dot{\gamma} \end{bmatrix} \tag{4}$$

$$\dot{\boldsymbol{\omega}} = \ddot{\alpha}\boldsymbol{e}_1^{(0)} + \ddot{\beta}\boldsymbol{e}_2^{(1)} + \dot{\alpha}\boldsymbol{e}_1^{(0)} \times \dot{\beta}\boldsymbol{e}_2^{(1)} + \ddot{\gamma}\boldsymbol{e}_3^{(2)} + \left(\dot{\alpha}\boldsymbol{e}_1^{(0)} + \dot{\beta}\boldsymbol{e}_2^{(1)}\right) \times \dot{\gamma}\boldsymbol{e}_3^{(2)} \tag{5}$$

$$= \begin{bmatrix} cos\beta cos\gamma & sin\gamma & 0 \\ -cos\beta sin\gamma & cos\gamma & 0 \\ sin\beta & 0 & 1 \end{bmatrix} \begin{bmatrix} \ddot{\alpha} \\ \ddot{\beta} \\ \ddot{\gamma} \end{bmatrix} + \dot{\alpha} \begin{bmatrix} 0 & -sin\beta cos\gamma & -cos\beta sin\gamma \\ 0 & sin\beta sin\gamma & -cos\beta cos\gamma \\ 0 & cos\beta & 0 \end{bmatrix} \begin{bmatrix} \dot{\alpha} \\ \dot{\beta} \\ \dot{\gamma} \end{bmatrix} + \dot{\alpha}\dot{\beta} \begin{bmatrix} cos\gamma \\ -sin\gamma \\ 0 \end{bmatrix}$$

The hybrid coordinate dynamical analysis method [30] is a popular method used to describe the translational motion of a rigid-flexible coupled multi-body system. There are two types of coordinate frames used in this method (see **Fig. 2**). One is the global reference frame $\boldsymbol{e}_g$, which describes the location of the bodies, and the other is the local elastic body-fixed frame (floating frame [38]) $\boldsymbol{e}_b$, which describes the deformations of the bodies.

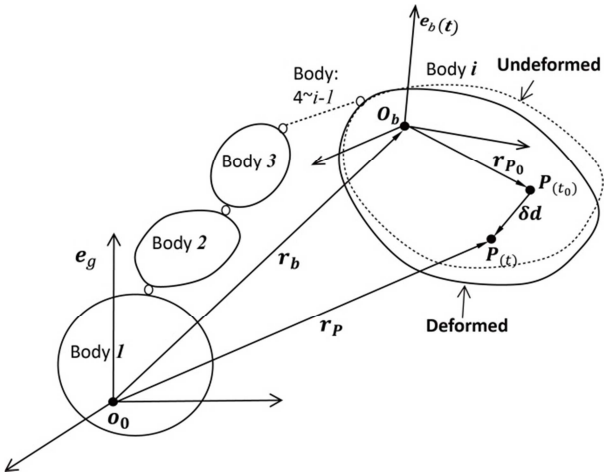

Fig. 2. Hybrid coordinate dynamic analysis method.

For example, as shown in **Fig. 2**, the position vector of the point $\boldsymbol{P}$ in the body i after deformation can be written as:

$$\boldsymbol{r_P} = \boldsymbol{r_b} + \boldsymbol{r_{P_0}} + \boldsymbol{\delta d} \tag{6}$$

where $\boldsymbol{\rho_{P_0}}$ is the position of the point $\boldsymbol{P}$ relative to its floating frame $\boldsymbol{e}_b(\boldsymbol{t})$ in the undeformed state. $\boldsymbol{\Delta U}$ is the deformation of the point $\boldsymbol{P}$. $\boldsymbol{r_b}$ is the radial vector between the origin of the global reference frame $\boldsymbol{e}_g$ and the origin of the floating frame $\boldsymbol{e}_b(\boldsymbol{t})$, which can be calculated via the path vectors between bodies.

According to Eq. (6), the velocity and acceleration of the point $\boldsymbol{P}$ can be written as follows:

$$\dot{\boldsymbol{r}}_{\boldsymbol{P}} = \dot{\boldsymbol{r}}_{\boldsymbol{b}} + \boldsymbol{\omega} \times \left(\boldsymbol{r_{P_0}} + \boldsymbol{\delta d}\right) + \boldsymbol{\delta}\underline{\dot{\boldsymbol{d}}} \tag{7}$$

$$\ddot{\boldsymbol{r}}_{\boldsymbol{P}} = \ddot{\boldsymbol{r}}_{\boldsymbol{b}} + \dot{\boldsymbol{\omega}} \times \left(\boldsymbol{r_{P_0}} + \boldsymbol{\delta d}\right) + 2\boldsymbol{\omega} \times \boldsymbol{\delta}\underline{\dot{\boldsymbol{d}}} + \boldsymbol{\omega} \times \left[\boldsymbol{\omega} \times \left(\boldsymbol{r_{P_0}} + \boldsymbol{\delta d}\right)\right] + \boldsymbol{\delta}\underline{\ddot{\boldsymbol{d}}} \tag{8}$$

where $\boldsymbol{\delta}\underline{\dot{\boldsymbol{d}}}$ and $\boldsymbol{\delta}\underline{\ddot{\boldsymbol{d}}}$ are the first- and second-order derivative of the deformation $\boldsymbol{\delta d}$ versus time with respect to the floating frame $\boldsymbol{e}_b(\boldsymbol{t})$, respectively.

In the code, flexible bodies (e.g., tower and blades) are modeled as Bernoulli-Euler beams and are divided into numerous structural elements. Deformations are calculated at the midpoint of the discrete elements using assumed mode method [39] as follows:

$$\boldsymbol{\delta d} = \left(\boldsymbol{\phi} + \frac{1}{2}\boldsymbol{A_Q}^T \cdot \boldsymbol{H}\right) \cdot \boldsymbol{Q} \tag{9}$$

where:

Spatial shape functions matrix:

$$\boldsymbol{\phi} = \begin{bmatrix} \boldsymbol{\phi_x}^T & \boldsymbol{0} & \boldsymbol{0} \\ \boldsymbol{0} & \boldsymbol{\phi_y}^T & \boldsymbol{0} \\ \boldsymbol{0} & \boldsymbol{0} & \boldsymbol{\phi_z}^T \end{bmatrix} \tag{10}$$

$$\begin{cases} \boldsymbol{\phi_x} = [\phi_{x1,} \quad \phi_{x2,} \quad \cdots \quad \phi_{xn}]^T \\ \boldsymbol{\phi_y} = [\phi_{y1,} \quad \phi_{y2,} \quad \cdots \quad \phi_{yn}]^T \\ \boldsymbol{\phi_z} = [\phi_{z1,} \quad \phi_{z2,} \quad \cdots \quad \phi_{zn}]^T \end{cases} \tag{11}$$

Generalized coordinate matrix:

$$\boldsymbol{Q} = [\boldsymbol{q_x}, \quad \boldsymbol{q_y}, \quad \boldsymbol{q_z}]^{\boldsymbol{T}} \tag{12}$$

$$\boldsymbol{A_Q} = [\boldsymbol{Q} \quad \boldsymbol{0} \quad \boldsymbol{0}] \tag{13}$$

$$\begin{cases} \boldsymbol{q_x} = [q_{x1,} \quad q_{x2,} \quad \cdots \quad q_{xn}]^T \\ \boldsymbol{q_y} = [q_{y1,} \quad q_{y2,} \quad \cdots \quad q_{yn}]^T \\ \boldsymbol{q_z} = [q_{z1,} \quad q_{z2,} \quad \cdots \quad q_{zn}]^T \end{cases} \tag{14}$$

Nonlinear coupling effect matrix:

$$\boldsymbol{H} = \begin{bmatrix} \boldsymbol{0} & \boldsymbol{0} & \boldsymbol{0} \\ \boldsymbol{0} & \boldsymbol{H_y} & \boldsymbol{0} \\ \boldsymbol{0} & \boldsymbol{0} & \boldsymbol{H_z} \end{bmatrix} \tag{15}$$

$$\begin{cases} \boldsymbol{H_y} = -\int_0^x \left(\frac{\partial \boldsymbol{\phi_y}}{\partial x}\right) \cdot \left(\frac{\partial \boldsymbol{\phi_y}}{\partial x}\right)^T dx \\ \boldsymbol{H_z} = -\int_0^x \left(\frac{\partial \boldsymbol{\phi_z}}{\partial x}\right) \cdot \left(\frac{\partial \boldsymbol{\phi_z}}{\partial x}\right)^T dx \end{cases} \tag{16}$$

where $\boldsymbol{\phi}$ is a spatial shape functions matrix. $\boldsymbol{\phi_x}$ is the *x*-axis component of $\boldsymbol{\phi}$, and ϕ_{xn} is the n[th] shape functions of $\boldsymbol{\phi_x}$. $\boldsymbol{Q}$ is the modal coordinates matrix. $\boldsymbol{q_x}$ is the *x*-axis component of $\boldsymbol{Q}$, and q_{xn} is the n[th] modal coordinates matrix of ϕ_{xn}. $\boldsymbol{H}$ is the geometric nonlinear coupled matrix [40], which accounts for the non-linear rigid-flexible coupled effects, e.g., the "dynamic stiffening effect", which has been investigated by the authors in the reference [41]. It is noted that the torsion and shear-related terms are deemed negligible and are not considered in the current code.

To describe the topological configuration of a FOWT, the adjacent array method proposed by Huston et al. [31] for an open chain multi-body system is used. As shown in **Fig. 3**, the global inertial frame is labelled B_0, the floating platform is labelled B_1, the tower is labelled B_2, the nacelle is labelled B_3, the shaft system is labelled B_4 and the three blades are labelled B_5, B_6 and B_7. After listing the sequence of the lower adjacent body of the B_1 – B_7 orderly, the adjacent array can be written as Eq. 17. It is convenient to describe the relationship of the bodies of a FOWT system using the adjacent array method. For example, we know the nacelle is the third body B_3 (see Fig. 3) and the value of the third element in the adjacent array is '2'. Hence, we can know that the lower adjacent body next to the nacelle is the tower B_2 (see Fig. 3), and so on.

$$L_a = [0 \quad 1 \quad 2 \quad 3 \quad 4 \quad 4 \quad 4]^T \tag{17}$$

A FOWT is a complex rigid-flexible coupling multi-body system. The state of motion of the bodies should be described in coordinate systems. The coordinate systems used in the code are shown in **Fig. 3**. The global inertial frame $\boldsymbol{e_g}$ is fixed at the interface between the still water level and the initial centreline of the floating platform. The floating platform frame $\boldsymbol{e_p}$ coincides with the $\boldsymbol{e_g}$ at the beginning but it translates and rotates with the platform. The tower-base frame (or the floating frame of the tower) $\boldsymbol{e_{tb}}$ is fixed at the bottom of the tower and is parallel to the platform frame $\boldsymbol{e_p}$. The tower-top frame $\boldsymbol{e_{tt}}$ and the nacelle frame $\boldsymbol{e_n}$ are coincident when the yaw angle of the nacelle is zero, but the $\boldsymbol{e_n}$ rotates with the nacelle. The shaft frame $\boldsymbol{e_s}$ does not rotate with the rotor but considers the shaft tilt angle. The hub frame $\boldsymbol{e_h}$ is located at the centroid of the hub and rotates with the rotor. The coned frame $\boldsymbol{e_c}$ and blade frame $\boldsymbol{e_b}$ are fixed at the root of a blade, considering the cone angle of the blade and rotating with the rotor. Note that the frame $\boldsymbol{e_b}$ pitches with the blade but the frame $\boldsymbol{e_c}$ does not.

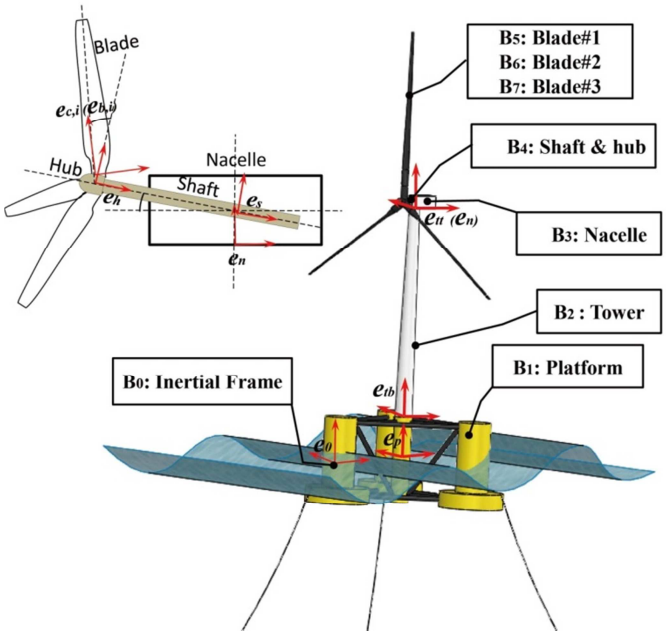

Fig. 3. Configuration and frames of a FOWT.

After all the coordinate systems are confirmed, the degrees of freedom (DOFs) of a FOWT can be defined as follows:

- Six floating platform DOFs $\boldsymbol{x}_{1\to6}^{\boldsymbol{P}}$, including three translational DOFs (surge, sway and heave) and three rotational DOFs (roll, pitch and yaw) between the platform frame $\boldsymbol{e}_p$ and the global inertial frame $\boldsymbol{e}_g$.
- Modal coordinates of deformations of the tower with respect to the tower-base frame $\boldsymbol{e}_{tb}$, including n-order fore-aft modal coordinates ($\boldsymbol{x}_{1\to n}^{\boldsymbol{Tfa}}$) and n-order side-to-side modal coordinates ($\boldsymbol{x}_{1\to n}^{\boldsymbol{Tss}}$) without considering the torsional deformations. The first 4 modes (2 fore-aft modes and 2 side-to-side modes) are considered in this paper.
- Yaw motion of the nacelle ($\boldsymbol{x}^{\boldsymbol{N}}$), which is used to describe the angle between the nacelle frame $\boldsymbol{e}_n$ and the tower-top frame $\boldsymbol{e}_{tt}$.
- Rotation of the rotor ($\boldsymbol{x}^{\boldsymbol{R}}$), which is defined as the angle between the hub frame $\boldsymbol{e}_h$ and the shaft frame $\boldsymbol{e}_s$.
- Three blades pitch angles ($\boldsymbol{x}_{1\to3}^{\boldsymbol{Bp}}$), which are defined as the angle between the blade frame $\boldsymbol{e}_b$ and the coned frame $\boldsymbol{e}_c$. In the current code, drivetrain torsion or bending are neglected and the drivetrain is modelled as a rigid body.
- Modal coordinates of deformations of the blades with respect to the blade frame $\boldsymbol{e}_b$, including n-order flapwise modal coordinates ($\boldsymbol{x}_{1\to n}^{\boldsymbol{Bf}}$) and n-order edgewise modal coordinates ($\boldsymbol{x}_{1\to n}^{\boldsymbol{Be}}$) without considering the torsional deformations. Øye [42] found that the first 3 or 4 modes (2 flapwise modes, 1 or 2 edgewise modes) used for a wind turbine were in good agreement with measurements. The first 3 modes (2 flapwise modes and 1 edgewise modes) are thus considered in this paper.

Finally, the DOFs array $\boldsymbol{X}$ is given by:

$$\boldsymbol{X} = \left[\boldsymbol{x}_{1\to6}^{\boldsymbol{P}},\ \boldsymbol{x}_{1\to n}^{\boldsymbol{Tfa}},\ \boldsymbol{x}_{1\to n}^{\boldsymbol{Tss}},\ \boldsymbol{x}^{\boldsymbol{N}},\ \boldsymbol{x}^{\boldsymbol{R}},\ \boldsymbol{x}_{1\to3}^{\boldsymbol{Bp}},\ \boldsymbol{x}_{1\to n}^{\boldsymbol{Bf}},\ \boldsymbol{x}_{1\to n}^{\boldsymbol{Be}}\right]^{\boldsymbol{T}} \tag{18}$$

After establishing the kinematical model using the above methods, the dynamical governing equations for the system are solved by Kane's dynamical equations. Kane's dynamical equations [28] have many advantages in solving the dynamic models for a multi-body system; for example, they eliminate the need to take the derivative of the dynamical functions or dispose of workless constraint forces and moments, which make it more computationally efficient compared with the other methods.. The DOFs array $\boldsymbol{X}$ is also called the generalized coordinates in Kane's dynamical method, and the first-order time derivative is called the generalized velocity in Kane's dynamical method.

The process of establishment using Kane's dynamical equations for a FOWT is shown in Fig. 4. First, the translational and angular velocities of the kinematic reference points (joints between bodies, conventionally) of the bodies are calculated, for example, body *i*, with consideration of the deformations of the body *i-1* and the relative motion between the bodies *i* and *i-1*. Then, with consideration of the deformations field and kinestate of the body *i*, the translational and angular velocities of the kinetic reference point (centre of mass of bodies, conventionally) of the body *i* are calculated as follows:

$$\dot{\boldsymbol{r}}_i = {}^{\boldsymbol{p}}\boldsymbol{V}_i \cdot \dot{\boldsymbol{X}} \tag{19}$$

$$\boldsymbol{\omega}_i = {}^{\boldsymbol{p}}\boldsymbol{W}_i \cdot \dot{\boldsymbol{X}} \tag{20}$$

where ${}^{\boldsymbol{p}}\boldsymbol{V}_{\boldsymbol{i}}$ is the partial velocity matrix of the kinetic reference point of the body *i* and ${}^{\boldsymbol{p}}\boldsymbol{\omega}_{\boldsymbol{i}}$ is the partial angular velocity matrix of the body *i*.

According to Eqs. (19) and (20), the translational and angular acceleration can be written as:

$$\ddot{\boldsymbol{r}}_i = {}^{\boldsymbol{p}}\boldsymbol{V}_{\boldsymbol{i}} \cdot \ddot{\boldsymbol{X}} + \boldsymbol{B}_i \tag{21}$$

$$\dot{\boldsymbol{\omega}}_i = {}^{\boldsymbol{p}}\boldsymbol{W}_{\boldsymbol{i}} \cdot \ddot{\boldsymbol{X}} + \boldsymbol{D}_i \tag{22}$$

where $\boldsymbol{B}_i$ and $\boldsymbol{D}_i$ are the remainder terms of the translational and angular acceleration, respectively; the terms are complicated but can be deduced from Eq. (8) and Eq. (5), respectively.

The general Kane's dynamical equation for the system is given by:

$$F + F^* = 0 \tag{23}$$

For a rigid-flexible-servo coupling multi-body system, the above equation can be expanded as:

$$\sum_{h=1}^{N_r}\left({}^{R}F_h + {}^{R}F_h^*\right) + \sum_{k=1}^{N_f}\left({}^{F}F_k + {}^{F}F_k^*\right) + \sum_{l=1}^{N_c}{}^{C}F_l = 0,\ (N_r + N_f + N_c = N \tag{24}$$

where ${}^{R}F_h$ and ${}^{R}F_h^*$ are the generalized active forces and generalized inertia forces for the h^{th} rigid body, ${}^{F}F_k$ and ${}^{F}F_k^*$ are the generalized active forces and generalized inertia forces for the k^{th} flexible body, and ${}^{C}F_l$ are the generalized active (internal) forces from the l^{th} control actuator.

The generalized active forces and generalized inertia forces for the system can be accumulated as:

$$F = \sum_{i=1}^{N_r+N_f}\left[\left({}^{\boldsymbol{p}}\boldsymbol{V}_{\boldsymbol{i}}\right)^T \cdot \boldsymbol{F}_{\boldsymbol{i}} + \left({}^{\boldsymbol{p}}\boldsymbol{W}_{\boldsymbol{i}}\right)^T \cdot \boldsymbol{M}_{\boldsymbol{i}} - E_i\right] + \sum_{l=1}^{N_c}\left[\left({}^{\boldsymbol{p}}\boldsymbol{V}_{\boldsymbol{l}}\right)^T \cdot \boldsymbol{F}_{\boldsymbol{l}} + \left({}^{\boldsymbol{p}}\boldsymbol{W}_{\boldsymbol{l}}\right)^T \cdot \boldsymbol{M}_{\boldsymbol{l}}\right] \tag{25}$$

$$F^* = -\sum_{i=1}^{N_r+N_f}\left\{\left({}^{\boldsymbol{p}}\boldsymbol{V}_{\boldsymbol{i}}\right)^T \cdot (m_i \cdot \ddot{\boldsymbol{r}}_{\boldsymbol{i}}) + \left({}^{\boldsymbol{p}}\boldsymbol{W}_{\boldsymbol{i}}\right)^T \cdot [I_i \cdot \dot{\boldsymbol{\omega}}_{\boldsymbol{i}} + \boldsymbol{\omega}_{\boldsymbol{i}} \times (I_i \cdot \boldsymbol{\omega}_{\boldsymbol{i}})]\right\} \tag{26}$$

where $\boldsymbol{F}_{\boldsymbol{i}}$ and $\boldsymbol{M}_{\boldsymbol{i}}$ are the forces and moments matrix acting on the kinetic reference point of the body *i*, respectively. m_i and I_i are the mass and moment of inertia of the body *i*, respectively. The first-term of the right-hand side of Eq. (25) is the generalized active forces for a combination of rigid bodies and flexible bodies. Compared with the rigid bodies, there is an additional structural deformations energy term E in the flexible bodies**.** The second-term of the right-hand side of Eq. (25) is the generalized active (internal) forces from the control actuators. The right-hand side of Eq. (26) is the generalized inertia forces for rigid bodies and flexible bodies. Note that flexible bodies are

dispersed into the numerous elements mentioned before and Kane's dynamical equations thus need to be established at each element.

Substituting Eqs. (21), (22), (25) and (26) into Eq. (24), Kane's dynamical equation for a rigid-flexible-servo coupling multi-body system is given by:

$$\sum_{i=1}^{N_r+N_f}\left[\left({}^{p}\boldsymbol{V}_i\right)^{T}\cdot\boldsymbol{F}_i+\left({}^{p}\boldsymbol{W}_i\right)^{T}\cdot\boldsymbol{M}_i-\boldsymbol{E}_i\right]+\sum_{l=1}^{N_c}\left[\left({}^{p}\boldsymbol{V}_l\right)^{T}\cdot\boldsymbol{F}_l+\left({}^{p}\boldsymbol{W}_l\right)^{T}\cdot\boldsymbol{M}_l\right]-$$
$$\sum_{i=1}^{N_r+N_f}\left[\left({}^{p}\boldsymbol{V}_i\right)^{T}\cdot m_i\cdot{}^{p}\boldsymbol{V}_i+\left({}^{p}\boldsymbol{W}_i\right)^{T}\cdot I_i\cdot{}^{p}\boldsymbol{W}_i\right]\cdot\ddot{\boldsymbol{X}}-\sum_{i=1}^{N_r+N_f}\left\{\left({}^{p}\boldsymbol{V}_i\right)^{T}\cdot m_i\cdot\boldsymbol{B}_i+\left({}^{p}\boldsymbol{W}_i\right)^{T}\cdot\right. \quad (27)$$
$$\left.[I_i\cdot\boldsymbol{D}_i+\boldsymbol{\omega}_i\times(I_i\cdot\boldsymbol{\omega}_i)]\right\}=\boldsymbol{0}$$

Let:

$$\boldsymbol{GM}=\sum_{i=1}^{N_r+N_f}\left[\left({}^{p}\boldsymbol{V}_i\right)^{T}\cdot m_i\cdot{}^{p}\boldsymbol{V}_i+\left({}^{p}\boldsymbol{W}_i\right)^{T}\cdot I_i\cdot{}^{p}\boldsymbol{W}_i\right] \quad (28)$$

$$\boldsymbol{GF}=\sum_{i=1}^{N_r+N_f}\left[\left({}^{p}\boldsymbol{V}_i\right)^{T}\cdot\boldsymbol{F}_i+\left({}^{p}\boldsymbol{W}_i\right)^{T}\cdot\boldsymbol{M}_i-\boldsymbol{E}_i\right]+\sum_{l=1}^{N_c}\left[\left({}^{p}\boldsymbol{V}_l\right)^{T}\cdot\boldsymbol{F}_l+\left({}^{p}\boldsymbol{W}_l\right)^{T}\cdot\boldsymbol{M}_l\right]-$$
$$\sum_{i=1}^{N_r+N_f}\left\{\left({}^{p}\boldsymbol{V}_i\right)^{T}\cdot m_i\cdot\boldsymbol{B}_i+\left({}^{p}\boldsymbol{W}_i\right)^{T}\cdot[I_i\cdot\boldsymbol{D}_i+\boldsymbol{\omega}_i\times(I_i\cdot\boldsymbol{\omega}_i)]\right\} \quad (29)$$

Eq. (27) indicates that Kane's dynamical equations are actually scalar equations. Therefore, Kane's dynamical equations for each body can be established with respect to different coordinate systems. Then, Kane's dynamical equation for the entire system is assembled by accumulating the dynamical equations from all components. In the end, the second-order derivative (acceleration) of the generalized coordinates (degrees of freedom) is solved by the system Kane's dynamical equation as:

$$\ddot{\boldsymbol{X}}=\boldsymbol{GM}^{-1}\cdot\boldsymbol{GF} \quad (30)$$

The generalized coordinates at the next time can be predicted by a time–marching scheme that will be detailed in later sections.

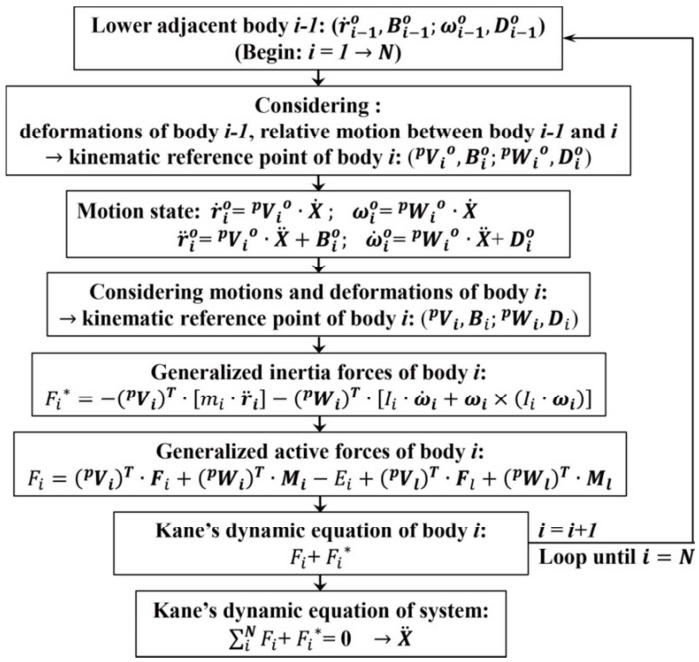

Fig. 4. Process of Kane's dynamical method for FOWTs

2.2. Aerodynamics

Aerodynamics are important for a FOWT in regard to aerodynamic loads, energy efficiency, fatigue damage, and other factors. A brief introduction to the aerodynamic loads calculation methods is described in this subsection.

The Blade Element/Momentum method (BEM) with aerodynamic corrections is currently applied in the code. The BEM was first proposed by Rankine [43] and Froude [44] in the 19th century and is generally attributed to Glauert [32] in the 20th century; it remains one of the most commonly used methods for calculating induced velocities and aerodynamic loads of wind turbines. In fact, it is a combination of 1-D momentum theory and 2-D blade element theory. In the momentum theory, the rotor is modelled as an ideal actuating disc without accounting for the actual geometry. The loss of momentum of the inflow results from the work done by the airflow passing through the rotor disc. In the blade element theory, it is assumed that the blades can be divided into two-dimensional airfoil sections, and aerodynamic loads are independently solved on each element. The aerodynamic loads derived from the 1-D momentum theory and the 2-D element model should be equal. There are in fact some drawbacks in the conventional BEM method used for FOWTs because of its simplifications [33]. Therefore, aerodynamic corrections have been taken to improve the accuracy of the BEM method in the code. For instance, the Prandtl's tip-loss and hub-loss corrections [33] is used to consider the vortices shed at these locations, the Glauert's correction is applied to take the large induction velocities into account [45], the skewed wake correction is used to consider the effects of incoming flow that is not perpendicular to the rotor plane [46], and the dynamic wake correction is used to consider the aerodynamic time delay effect [47]. Nevertheless, the hysteresis loops effect is not considered in the current code. A flow chart of the aerodynamic calculation in the code is shown in **Fig. 5**. As seen, the solution for the aerodynamic induction factors is an iteration [33]. When the aerodynamic induced factors all converge or reach the cyclic upper limit, the iteration stops and the skewed wake correction method, and the dynamic wake correction method are used to correct the aerodynamic induced factors, if needed. For conciseness and clarity, the derivations of the BEM and the corrections mentioned above are not detailed in this paper.

The aerodynamic loads of the tower are calculated by accumulating the aerodynamic load at the midpoints of all discrete elements by:

$$d\boldsymbol{F}^{\boldsymbol{T}} = \frac{1}{2}\rho C_d \delta L D (\boldsymbol{V}_{\boldsymbol{0}}^{\boldsymbol{wind}} - \boldsymbol{V}_{\boldsymbol{TE}}) \left| \boldsymbol{V}_{\boldsymbol{0}}^{\boldsymbol{wind}} - \boldsymbol{V}_{\boldsymbol{TE}} \right| \tag{31}$$

where C_d is the drag coefficient ($C_d = 0.5$ along the tower in this paper). D is the diameter of the local tower section, $\boldsymbol{V}_{\boldsymbol{0}}^{\boldsymbol{wind}}$ is the upstream wind speed, and $\boldsymbol{V}_{\boldsymbol{TE}}$ is the motion velocity considering the influences from the supporting platform and the tower's vibration.

The wind field can be considered in the code as steady wind or turbulent wind. Turbulent wind is pre-processed by the turbulent-wind simulator TubSim [48] by NREL and then is interpolated (linear interpolation) in the code according to the current time and the location of the blade element.

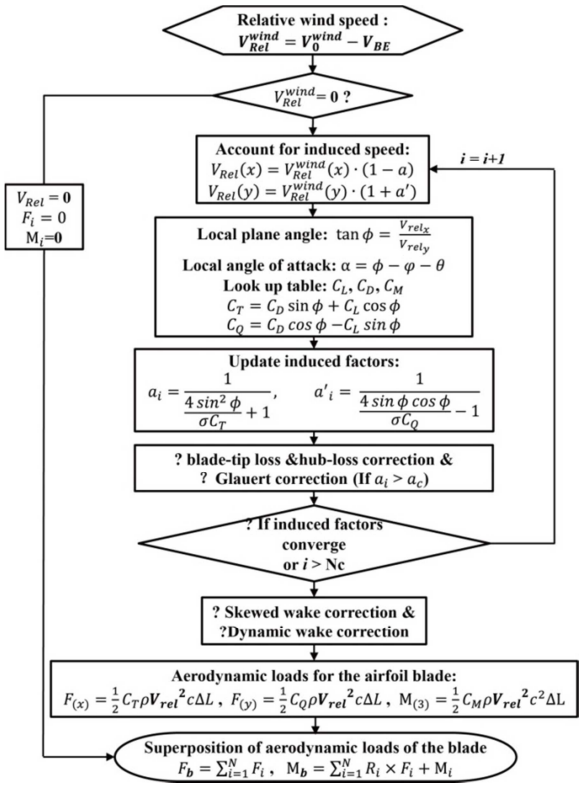

Fig. 5. Flow chart of the aerodynamic calculation.

2.3. Hydrodynamics

The floating supporting platform of a FOWT is sensitive to hydrodynamic loads. The relevant hydrodynamic methodologies used in the code are thus introduced in this subsection.

Airy wave theory [34] is used to describe wave kinematics in the code. In this linear wave theory, the hydrodynamic problem can be split into three separate problems: diffraction, radiation and hydrostatics [34, 49]. In practice, a three-dimensional panel-based hydrodynamic analysis program, *WAMIT* (Wave Analysis at Massachusetts Institute of Technology) [50], is used to output hydrodynamic coefficients in the frequency-domain (e.g., hydrostatic restoring forces coefficients, wave excitation coefficients, radiation coefficients and quadratic transfer functions). These hydrodynamic coefficients are then loaded into the DARwind code, which generates time-domain hydrodynamic loads according to the desired sea states. It is noted that the linear wave theory is based on the assumption that the amplitudes of the incident waves are much smaller relative to its wavelengths and the range of motion of a floating platform are smaller than its characteristic body length. Otherwise, the hydrodynamic loads based on the linear wave theory will become less accurate. Fortunately, the assumption is appropriate for the floating offshore wind turbine in most cases. A similar discussion and similar theoretical framework of hydrodynamics of floating wind turbines can refer to the reference [51].

The time-domain excitation load on the support platform from incident waves can be calculated by the harmonic superposition method, as follows:

$$\boldsymbol{F^w} = \Re\left\{\sum_{j=1}^{N} H(\omega_j)\tilde{\zeta}_j e^{i\omega_j t}\right\} \tag{32}$$

where ω_j is the j^{th} frequency of regular wave components, $H(\omega_j)$ is the frequency response function associated with ω_j, $\tilde{\zeta}_j$ is the j^{th} complex-valued wave component amplitude (including phase), and

$\mathfrak{R}$ denotes the real value of the argument.

Second-order wave forces [52] are important for some FOWTs, e.g., semi-submersible FOWTs and tension leg FOWTs. The second-order wave force consists of difference-frequency and sum-frequency wave forces components, given by:

$$\boldsymbol{F}_{\boldsymbol{sec}}^{\boldsymbol{w}} = \mathfrak{R}\sum_{m}\sum_{n}\tilde{\zeta}_m\,\tilde{\zeta}_n^{*}\,H_{m,n}^{(2-)}e^{i(\omega_m-\omega_n)t} + \mathfrak{R}\sum_{m}\sum_{n}\tilde{\zeta}_m\,\tilde{\zeta}_n\,H_{m,n}^{(2+)}e^{i(\omega_m+\omega_n)t} \tag{33}$$

where $H_{m,n}^{(2-)}$ and $H_{m,n}^{(2+)}$ are the quadratic transfer functions (QTF) for the difference-frequency and sum-frequency forces, respectively. The asterisk (*) denotes the complex conjugate. The difference-frequency second-order wave forces can also be simplified using the Newman's approximation approach [53].

The linear wave radiation force with free-surface memory effects is given by:

$$\boldsymbol{F}_{\boldsymbol{j}}^{\boldsymbol{R}}(\boldsymbol{t}) = -\sum_{k=1}^{6}\left\{\mu_{jk}(\infty)\ddot{x}_k(t) + \int_{-\infty}^{t}K_{jk}(t-\tau)\dot{x}_k(\tau)d\tau\right\},\ \ j = 1,2,\dots,6 \tag{34}$$

where $\mu_{jk}(\infty)$ is the added mass coefficient at the infinite frequency, the second term of the right-hand side of the equation is the potential damping, and $K_{jk}(t-\tau)$ is the retardation function for the convolution integral accounting for the free-surface memory effect.

Buoyancy and hydrostatic restoring forces are calculated by:

$$\boldsymbol{F}^{\boldsymbol{s}} = [0 \quad 0 \quad \rho g V_0 \quad 0 \quad 0 \quad 0]^T - \boldsymbol{C}\cdot\boldsymbol{X} \tag{35}$$

where the first term represents the buoyancy and the second term represents the hydrostatic restoring forces. ρ is the fluid density, V_0 is the displaced volume of the fluid, and $\boldsymbol{C}$ is the linear hydrostatic-restoring coefficients matrix that depends on the water-plane area and the centre of buoyancy. $\boldsymbol{X}$ is the 6-DOFs motion matrix.

Because the hydrodynamic damping calculated by WAMIT does not account for viscous damping effects, it should be corrected using the Morison formula or the constant damping coefficient matrix (linear and quadratic damping coefficient matrix) in the code. The horizontal nonlinear viscous-drag force $d\boldsymbol{F}_{\boldsymbol{f}}^{\boldsymbol{V}}$ on a strip of dz is calculated using the Morison formula as:

$$d\boldsymbol{F}_{\boldsymbol{f}}^{\boldsymbol{V}} = -\frac{1}{2}\rho_w C_D D dz\cdot(\boldsymbol{v_w}-\boldsymbol{v_s})\cdot|\boldsymbol{v_w}-\boldsymbol{v_s}| \tag{36}$$

where C_D is the drag coefficient for the strip, D is the diameter of the strip, and $\boldsymbol{v_w}$ and $\boldsymbol{v_s}$ are the horizontal undisturbed water particle velocity and horizontal velocity of the strip, respectively. The total drag is the accumulation of drags on the immersed strips at instantaneous positions in the code.

Hydrodynamic damping can also be corrected by a damping matrix that includes a linear damping coefficient matrix and a quadratic damping coefficient matrix:

$$\boldsymbol{F}^{\boldsymbol{V}} = -\boldsymbol{C_{LD}}\cdot\dot{\boldsymbol{X}} - \boldsymbol{C_{SD}}\cdot\dot{\boldsymbol{X}}\cdot|\dot{\boldsymbol{X}}| \tag{37}$$

where $\boldsymbol{C_{LD}}$ is the linear damping coefficient matrix and $\boldsymbol{C_{SD}}$ is the quadratic damping coefficient matrix.

The Morison formula is generally more accurate than the constant damping coefficient matrix, but the drag coefficient $\boldsymbol{C_d}$ in the Morison formula depends on some empirical parameters [34] such as the Keulegan-Carpenter number, the Reynolds number and the surface roughness ratio. It is sometimes hard to confirm the C_d for all immersed components of a FOWT. Therefore, the constant damping coefficient matrix mentioned above could be more convenient sometimes.

The total hydrodynamic loads acting on the floating platform of a FOWT can thus be written as:

$$\boldsymbol{F_H} = \boldsymbol{F^w} + \boldsymbol{F_{sec}^w} + \boldsymbol{F^R} + \boldsymbol{F^s} + \boldsymbol{F^V} \tag{38}$$

2.4. Mooring system modelling

The mooring system is one of important means of holding an offshore structure against wind, waves and current. A quasi-static approach [36] used for a catenary mooring system is applied in the code, and the relevant methodologies are detailed in this subsection.

In this method, it is assumed that mooring lines are in static equilibrium at any time. The stretching of a mooring line is considered but dynamical characteristics (e.g., the inertia and damping), line bending stiffness and seabed friction are neglected.

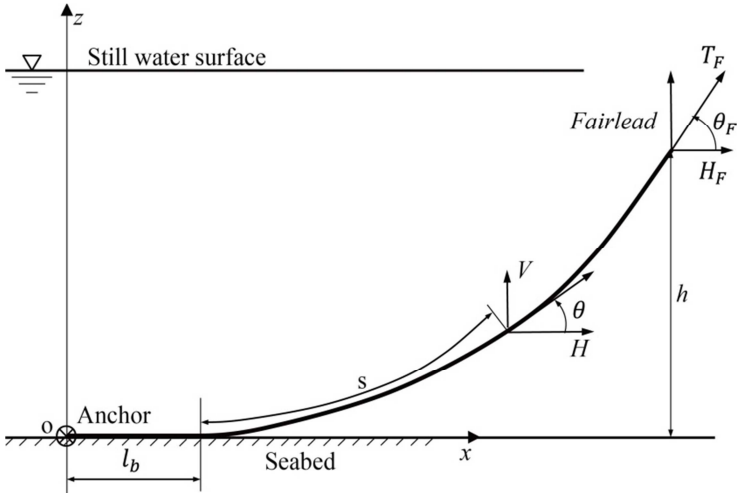

Fig. 6. Catenary mooring system.

When part of the anchor lines lie on the seabed, in other words, $l_b \neq 0$ (see **Fig. 6**), the vertical tensile force on the anchor is zero. Dynamic governing equations for a mooring line catenary are:

$$f_1 = L - \frac{V_F}{w} + \frac{H}{w} \cdot \ln \frac{V_F + \sqrt{V_F^2 + H^2}}{H} + \frac{H \cdot L}{EA} - x_F = 0 \tag{39}$$

$$f_2 = \frac{1}{w}\left(\sqrt{V_F^2 + H^2} - H\right) + \frac{w{l_s}^2}{2EA} - z_F = 0 \tag{40}$$

where x_F and z_F are the horizontal and vertical distance between the positions of the fairlead and the anchor of a line, respectively. H and V_F are the horizontal and vertical tensile forces on the fairlead, respectively. L is the unstretched length of a mooring line, w is the mooring line weight per unit length in water, EA is the extensional stiffness, and l_s is the impending segment of a line. Extension deformations of a line are considered with a horizontal extension $\frac{H \cdot L}{EA}$ and a vertical extension $\frac{w{l_s}^2}{2EA}$.

When l_b is zero, in other words, the vertical tensile force on the anchor V_A could be greater than zero:

$$V_A = V_F - wL \tag{41}$$

The dynamic governing equations of a mooring line are now rewritten as follows:

$$f_1 = \frac{H}{w} \cdot \ln \frac{V_F + \sqrt{V_F^2 + H^2}}{V_F - wL + \sqrt{(V_F - wL)^2 + H^2}} + \frac{H \cdot L}{EA} - x_F = 0 \tag{42}$$

$$f_2 = \frac{1}{w}\left(\sqrt{V_F^2 + H^2} - \sqrt{(V_F - wL)^2 + H^2}\right) + \frac{1}{EA}\left(V_F - \frac{wL}{2}\right) \cdot L - z_F = 0 \tag{43}$$

The above non-linear dynamic governing equations for the mooring lines can be solved by iteration

methods, for example, the Newton-Raphson iteration scheme, as follows:

$$\begin{bmatrix} H \\ V_F \end{bmatrix}_{n+1} = \begin{bmatrix} H \\ V_F \end{bmatrix}_n - \begin{bmatrix} \frac{\partial f_1}{\partial H} & \frac{\partial f_1}{\partial V_F} \\ \frac{\partial f_2}{\partial H} & \frac{\partial f_2}{\partial V_F} \end{bmatrix}_n^{-1} \cdot \begin{bmatrix} f_1 \\ f_2 \end{bmatrix}_n \tag{44}$$

In some FOWTs, e.g., Hywind, the mooring lines are similar to those in **Fig. 7**, the so-called "crowfoot" [54] used to improve the yaw stiffness of a mooring system. A mooring line can be divided into three elements: element#1, element#2 and element#3 (see **Fig. 7**). Each element is solved as for a single catenary line, mentioned before. Additionally, force-balance equations should be satisfied at the joint node of these connective elements, as follows:

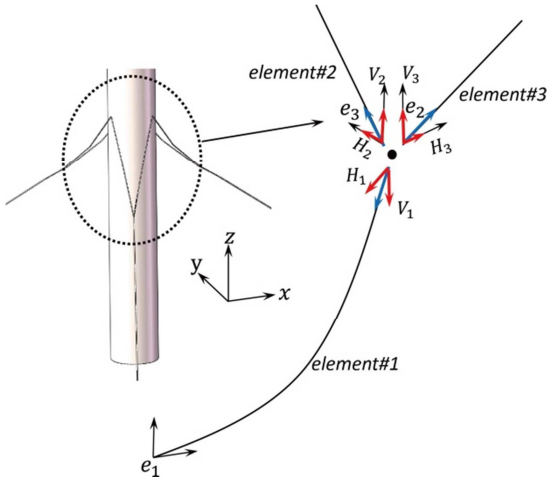

Fig. 7. Solution for a multi-segmented mooring system.

$$\begin{cases} \left(\sum_{i=1}^{3} H_i \cdot \cos\alpha_i\right) - F_x^{ext} = 0 \\ \left(\sum_{i=1}^{3} H_i \cdot \sin\alpha_i\right) - F_y^{ext} = 0 \\ \left(\sum_{i=1}^{3} V_i\right) - F_z^{ext} = 0 \end{cases} \tag{45}$$

where H_i and V_i are horizontal and vertical tensile forces of the i^{th} elements, respectively, α_i is the angle of a rotation around the global z-axis, which describes the relationship between the local frame of the i^{th} element and the global frame, and F^{ext} is the external load on the joint node. It is hard to calculate the Jacobian matrix of the Newton-Raphson iteration for Eq. (45), and the secant method and the dichotomy method are thus used in the code. Although convergence speed using the secant method is fast, there is a possible numerical diffusion when the platform undergoes a large overall motion. In contrast, the dichotomy method is more robust. To speed up the dichotomy method, the iterative initial value at each time is set as the convergent value acquired at the last time. A similar approach can be found in reference [35].

2.5. Control strategies

The control strategies in the current code mainly refer to the work of Jonkman [55] and consist of a

generator-torque controller and a full-span rotor-collective blade-pitch controller. The generator-torque controller is mainly used to maximize power capture below the rated wind speed conditions. The blade-pitch controller is mainly used to regulate generator speed and electrical power above the rated wind speed conditions.

The generator torque is a tabulated function of the filtered generator speed in the code and includes five control regions, 1, 1½, 2, 2½, and 3, as shown in **Fig. 8**. In region 1, the actual wind speed below the cut-in value ($v < v_{cut-in}$) is used to accelerate the rotor. In the meantime, the generator torque is maintained at zero and energy harvesting is close. In region 1½, the wind speed begins to exceed the cut-in value ($v_{cut-in} \leq v < v_{rated}$) and energy harvesting starts. At this time, the generator torque is linearly controlled and is associated with the generator speed as a transition between the control region 1 and 2. In region 2 ($v_{cut-in} < v < v_{rated}$), the generator torque is proportional to the square of the filtered generator speed and achieves an optimal tip-speed ratio to maximize the power capture from the wind. Region 2½ ($v_{cut-in} < v < v_{rated}$) is a linear transition between regions 2 and 3, and the slope depends on the rated torque to the rated generator slip percentage. In region 3, the wind speed reaches or exceeds the rated conditions but is smaller than the cut-out value ($v_{\text{rated}} \leq v \leq v_{cut-out}$). The controller hold the generator torque constant at its nominal value, and the blade-pitch controller begins to regulate the power and generator speed. When the wind speed exceeds the cut-out value ($v > v_{cut-out}$), blades angle is feathered to minimize the aerodynamic loads and then the wind turbine shuts down.

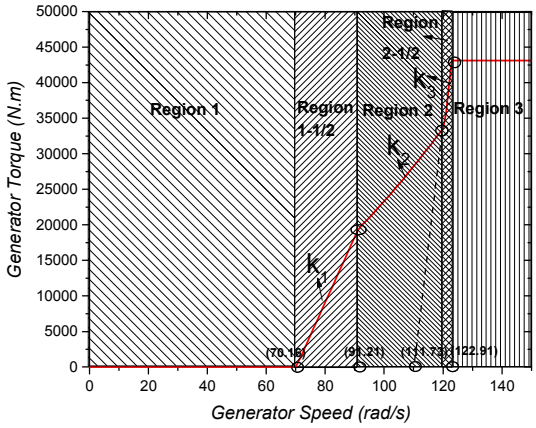

Fig. 8. Generator-torque controller.

A full-span rotor-collective blade-pitch controller with gain-scheduled and proportional-integral (PI) control based on the filtered generator speed error is used to regulate the generator speed and electrical power above the rated operation:

$$\Delta\theta = K_P \Delta\Omega + K_I \int_0^t \Delta\Omega \, dt \tag{46}$$

where K_P and K_I are the blade-pitch controller proportional and integral gains, respectively. These gains are adjusted over time according to the pitch angle of the blades. More details in regard to the control strategies can be found in the work of Jonkman [55].

2.6. Flow chart of the procedure

The current DARwind code is written in the FORTRAN language, and the code procedure is

illustrated in **Fig. 9**. As seen, all kind of loads, e.g., hydrodynamic loads, aerodynamic loads, mooring loads, and gravitational forces, are calculated at each time step according to the state of motion of the system. Subsequently, the derivatives of the generalized coordinates (accelerations) are calculated using Kane's dynamical equations. Finally, the displacement and velocity at the next time step are calculated using the classical Runge-Kutta method. The process described above is repeated until the terminative time. Compared with other existing software, it is more convenient to simulate FOWTs as different models in DARwind. For example, the FOWT system can be modeled as a single rigid body system for less time cost, modeled as a multi-rigid-body system for a balance of time cost and computational accuracy, or modeled as a rigid-flexible coupling multi-body system with or without considering nonlinear rigid-flexible coupled effects for accurate simulations but with the most time cost.

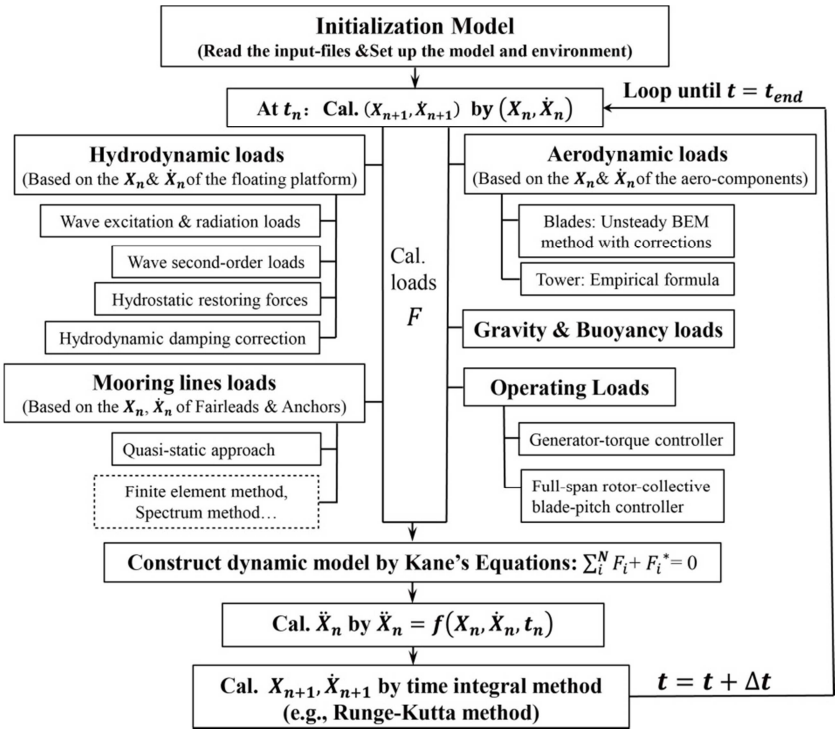

Fig. 9. Flow chart of the code.

3. Preliminary work

The theoretical background was presented previously. The remainder of this paper will emphasize the verification of the feasibility of the methods. Prior to the verifications, this subsection presents some preliminary work: the introduction of the experimental model, the comparison of decay tests, and the presentation of the load cases used for the following tests.

3.1. Experimental model

Experimental data of a FOWT model test will be used to verify the DARwind code in Section 4. A brief description of this experiment is given in this subsection. The experiment was conducted at the Deepwater Offshore Basin of the Shanghai Jiao Tong University using a DeepCwind semi-submersible FOWT [56, 57], as shown in **Fig. 10**. Some properties measured in the experiment are listed in **Table 1**. More details on the test executions, such as the model blades fabrication, wind field tests, the restoring tests of the mooring system and so on can be found in the references [11, 58, 59].

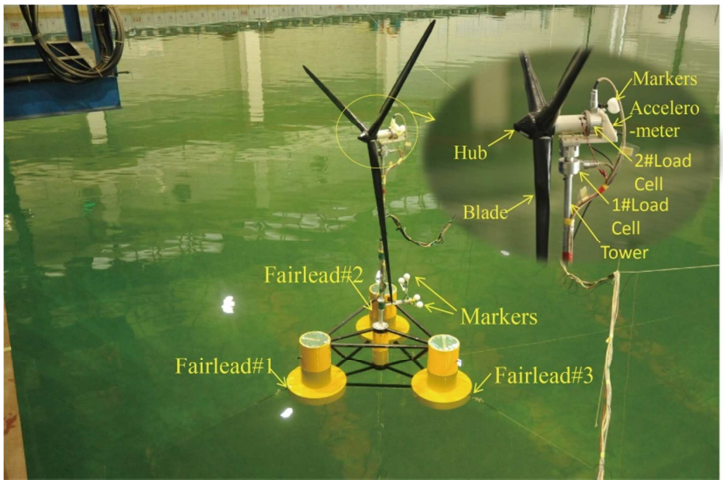

Fig. 10. Experimental model and sensors.

Table 1

Main properties of the experimental FOWT at full-scale.

Item	Measurements
Blades & Hub (kg)	109,931
Nacelle (kg)	232,291
Tower (kg)	287,128
Platform with ballast (kg)	12,878,750
Platform centre of mass (m)	-13.52
Platform roll & pitch inertia（kg.m^2）	6.31 E+09
Radius & depth of an anchor (m)	853.72; 200
Radius & depth of a fairlead (m)	40.87; 14
Diameter of a line (m)	0.0766
Unstretched length of a line (m)	835.5
Extensional stiffness (N)	7.35E+08
Unit weight of lines in fluid (kg/m)	105.975

3.2. Decay tests

It is hard to empirically determine the drag coefficient of the submersed components in the Morison formula because the platform of a semi-submersible FOWT consists of many trusses and pontoons with different size. In view of this point, the quadratic damping matrix, instead of the Morison formula, was used to improve the hydrodynamic damping of the numerical model according to the decay comparisons in practice:

$$\boldsymbol{C_{SD}} = \begin{bmatrix} 5.0\times10^{6} & 0 & 0 & 0 & 0 & 0 \\ 0 & 5.0\times10^{6} & 0 & 0 & 0 & 0 \\ 0 & 0 & 1.8\times10^{6} & 0 & 0 & 0 \\ 0 & 0 & 0 & 4.3\times10^{10} & 0 & 0 \\ 0 & 0 & 0 & 0 & 4.3\times10^{10} & 0 \\ 0 & 0 & 0 & 0 & 0 & 3.6\times10^{10} \end{bmatrix} \quad (47)$$

Natural frequencies and damping ratios for the 6-DOF motions between the experiment and code are listed in **Table 2**. In general, there was good agreement between the experiment and the code.

Table 2

Comparison of natural frequencies and damping ratios.

	Experiment		DARwind	
Motion Mode	Frequency (Hz)	Damping Ratio	Frequency (Hz)	Damping Ratio
Surge	0.0173	0.0260	0.0175	0.0119
Sway	0.0174	0.0282	0.0177	0.0164
Heave	0.0604	0.0115	0.0601	0.0122
Roll	0.0417	0.0127	0.0593	0.0076
Pitch	0.0413	0.0202	0.0409	0.0156
Yaw	0.0206	0.0115	0.0207	0.0110

3.3. Test matrix

The load cases for the following verification works are shown in **Table 3**. The irregular wave cases are based on the JONSWAP wave spectrum, wherein *Hs* represents the significant wave height, *Tp* represents the spectral peak wave period, and γ represents the spectral peak parameter. The duration of the cases are listed in the last column of the table. Note that the winds and waves were collinear and the heading was fixed at *0°* during the tests. Most verifications in the following tests were conducted by means of code-to-experiment comparisons. However, some quantities could not be measured in the experiment, for example, elastic deformations of the blades and the tower, dynamic responses with active controllers, and etc. Therefore, small amounts of quantities were verified by code-to-code comparisons (DARwind to FAST). More code-to-code comparisons between DARwind and FAST can be found in the supporting literature [60].

Table 3

Test matrix.

Load Case	Wind speed (m/s)	Rotor speed (rpm)	Wave parameter			Duration (s)
			Hs (m)	*Tp* (s)	γ	
LC1	9.4	7.9	-	-	-	1,500
LC2	12.8	14.42	-	-	-	1,500
LC3	12.8	14.42	4	10	-	1,500
LC4	0	0	2	8	3.3	3,600

4. Verifications and Discussion

A series of verification works were conducted to test the feasibility of the developed code, including the mooring system module, the structural elasticity module, the aerodynamic module, the hydrodynamic module, and the control strategy module and are reported in this section.

4.1. Mooring system

The mooring lines force-displacements of the experiment and the code are compared in **Fig. 11**. As

seen, there was good agreement within the range. On the other hand, the average tensile forces of the Fairlead#1 and Fairlead#2 (defined in **Fig. 10**) between the experiment and the code in wind-only cases (LC1 and LC2, see **Table 3**) are compared in **Fig. 12**, which shows that the average tensile forces of the fairleads between the experiment and the code were in good agreement and that the transition tendency from LC1 to LC2 was similar.

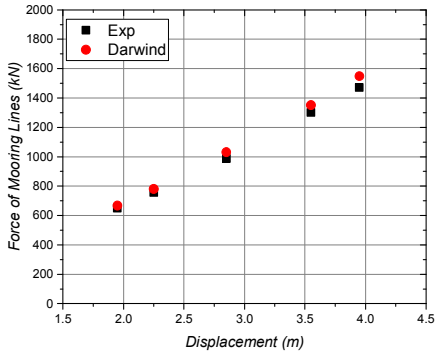

Fig. 11. Comparison of mooring lines force-displacement.

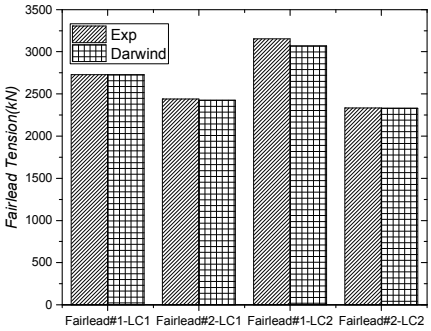

Fig. 12. Comparison of fairleads tension in wind-only cases.

The tensile forces of the Fairlead#1 over time between the experiment and the code in the combined wind and regular wave case (LC3, see **Table 3**) and the irregular wave case (LC4, see **Table 3**) are compared in **Fig. 13 (a)** and **(b)**, respectively. The figures demonstrate that the mean values of the fairlead tension force between the experiment and the code were similar but the volatility was different. It is obvious that the volatility of the fairlead tension in the code was smaller than that in the experiment, which possibly underestimated the extreme values of the mooring line tensions, fatigue damages, and the inherent responses of the floating platform. This difference is because of the lack of some dynamic effects; for example, the inertia and damping of the mooring lines were neglected in the quasi-static mooring modelling method in the code. Therefore, appropriate dynamic mooring system methods are suggested for development in the future, such as the lumped mass method and the finite element method.

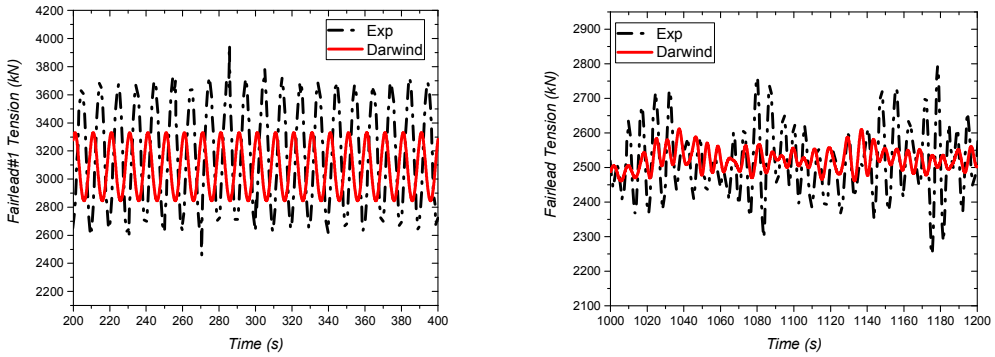

(a) (b)

Fig. 13. Comparison of the fairlead tensions in: (a) LC3; (b) LC4.

4.2. Structural elasticity

The FOWT is a complex rigid-flexible coupled multi-body system with a slender tower and blades. It is thus significant to accurately emulate structural elasticity in simulations. Because the structural elasticities of the tower and blades of the FOWT were not measured in the experiment, the code-to-code comparison was used as an alternative. The first bending natural frequencies of a blade in the flapwise direction at different rotor speeds predicted by the codes DARwind and FAST are compared in **Fig. 14**. The figure shows a good agreement between the results of the two numerical codes. For the tower, the first natural frequency in fore-aft direction predicted by DARwind was 0.3899 Hz and that predicted by FAST was 0.3566 Hz. The discrepancy in the tower frequency was also small.

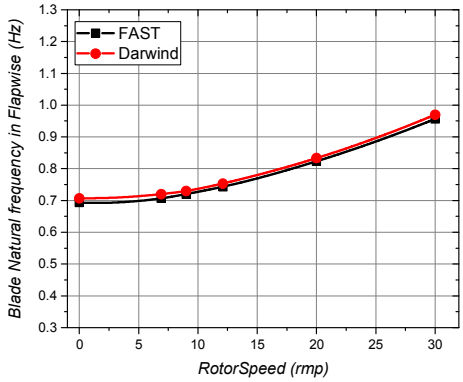

Fig. 14. Blade first bending natural frequency.

Deformations of the blade-tip and tower-top when the FOWT was subjected to the wind-only cases (LC1 and LC2 see **Table 3**, the platform was fixed to remove the influences from 6-DOFs motion, and the controllers were closed here) are compared in **Table. 4**. 'BTipDx' in the table is the deformation of the blade-tip in the flapwise direction. 'TTipDx' is the deformation of the tower-top-tip in the fore-aft direction. There is no significant difference between the results of the two codes, and it can be concluded that the structural elasticity of the code DARwind is feasible.

Table 4

Comparison of average elastic deformations between codes in LC1 and LC2.

Load Cases	LC1 (9.4 m/s-7.9 rpm)		LC2 (12.8 m/s-14.42 rpm)	
Codes	DARwind	FAST	DARwind	FAST
BTipDx /m	3.025	3.091	6.660	6.500
TTipDx /m	0.160	0.175	0.372	0.413

4.3. Aerodynamic performance

Aerodynamic loads between the codes DARwind and FAST in the wind-only cases (LC1 and LC2, see **Table 3**) are compared in **Table 5** (the floating platform was fixed here to remove the influences from the 6-DOFs motion, and the controllers were closed as well). In general, the differences between the two codes are not obvious. The small difference was likely due to the different aerodynamic methods (e.g., Glauert's correction and the skewed wake correction) used in the two codes.

Table 5

Comparison of mean aerodynamic loads between codes.

Load Case	LC1 (9.4 m/s-7.9 rpm)		LC2 (12.8 m/s-14.42 rpm)	
Codes	DARwind	FAST	DARwind	FAST
Thrust / kN	408.28	415.09	981.48	956.32
Torque /kN.m	3,239.86	3,242.68	5,404.90	5,156.49

Dynamical responses predicted by DARwind and those measured in the experiment are compared in **Figs. 15** and **16** for the cases when the floating platform was moored and subjected to the wind-only cases (LC1 and LC2, see **Table 3**). The figures show that the average platform motion (surge and pitch) predicted by DARwind were close to the experimental results. Nevertheless, there are some differences in fluctuation. In general, the motion fluctuation in the experiment is more irregular, which is likely caused by the more complicated aerodynamic-motion-mooring coupled effects or caused by more or less variation of the wind in the basin model test in practice.

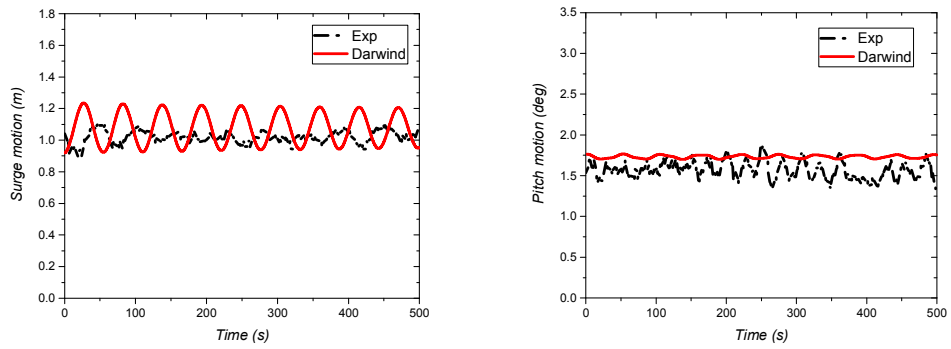

(a) (b)

Fig. 15. In LC1: (a) Surge motion; (b) Pitch motion.

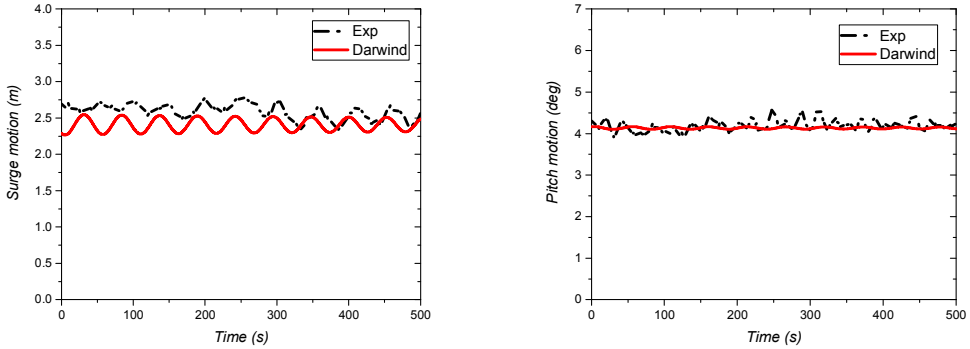

(a) (b)

Fig. 16. In LC2: (a) Surge motion; (b) Pitch motion.

4.4. Hydrodynamic performance

A comparison of the experiment and the code for the combined wind and regular wave case (LC3, see **Table 3**) is shown in **Fig. 17**. The figure shows that the wave elevation and the dynamic responses (surge and pitch) predicted by the code were similar to those generally measured in the experiment. Nonetheless, there was a small discrepancy in the average motion, likely because the BEM method used for the aerodynamic calculation in the code was insufficient when the floating platform of the FOWT underwent large overall motion and resulted in smaller average motion. The pitch motion experimental results seem to be different than a purely periodic response a bit, which is mainly caused by more or less turbulence of the wind in the basin model test in practice.

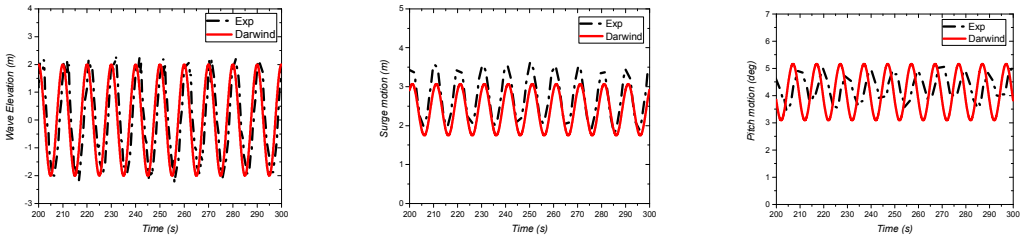

(a) (b) (c)

Fig. 17. In LC3: (a) Wave elevation; (b) Surge motion; (c) Pitch motion.

The power spectral densities of the wave elevations in the irregular wave case (LC4) are compared in **Fig. 18a**. As seen, there was good agreement between the measurements of the experiment and those predicted by the code. The power spectral density of the motion (surge and pitch) for LC4 are compared in **Fig. 18b** and **c**. An apparent fluctuation at the natural frequency and within the wave-frequency domain can be seen in the experiment and simulation. Nonetheless, the inherent responses predicted by the code were slightly smaller than those measured in the experiment. The reason is multifactorial: (i) the quasi-static mooring lines modelling method used in the code ignored the dynamic effects, which probably resulted in smaller inherent responses of the FOWT; and (ii) another possible reason is because of the nonlinear hydrodynamic damping effects. Although a quadratic damping matrix was used in the simulation, it was likely not perfect in practice.

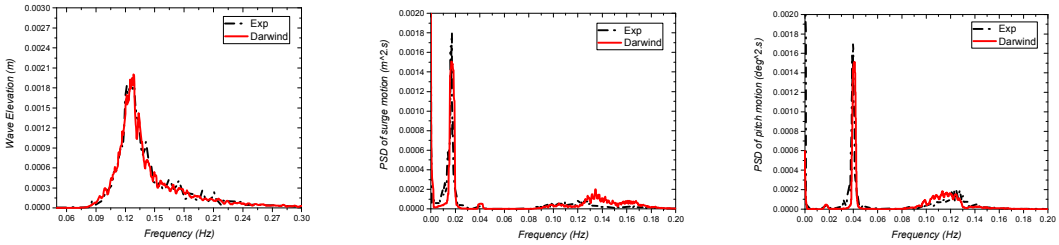

(a) (b) (c)

Fig. 18. In LC4: (a) Wave elevation; (b) Surge motion; (b) Pitch motion.

4.5. Control strategy

Tests of the controller strategy used in the code are reported in this section. Because the controllers were not included in the experiment, only the results of numerical analysis were used to make the code-to-code comparisons (DARwind and FAST).

As seen in **Fig. 19** (the wind-only case with wind speed of 11.4 m/s), the performances of the controllers between the two codes were similar and showed an ability to regulate the rotor speed and rotor power. Nonetheless, compared with FAST, the fluctuation of the rotor power in DARwind was greater, which resulted from the discrepancy in the generator-torque control algorithm between the two codes. In FAST, a multi-variable controller (a combination of the generator-torque controller and the blade-pitch controller) were used to stabilize the power above the rated operation [61], which achieved better performance in both rotor speed and electrical power regulation but likely gave rise to the variation of the generator torque and the fatigue damage of the shaft. In DARwind, the typical mono-variable control scheme is used when above the rated operation. At that time, the generator-torque controller maintained the nominal torque, only making the blade-pitch controller to regulate the power and rotor speed, which gave rise to the rotor power variation, as shown in **Fig. 19 (b)**. We suggest that a more advanced control strategy to mitigate both the variations of generator torque and the power should be developed in the future, for example, the individual pitch controller, the tuned mass damper controller, the neural network controller and so on.

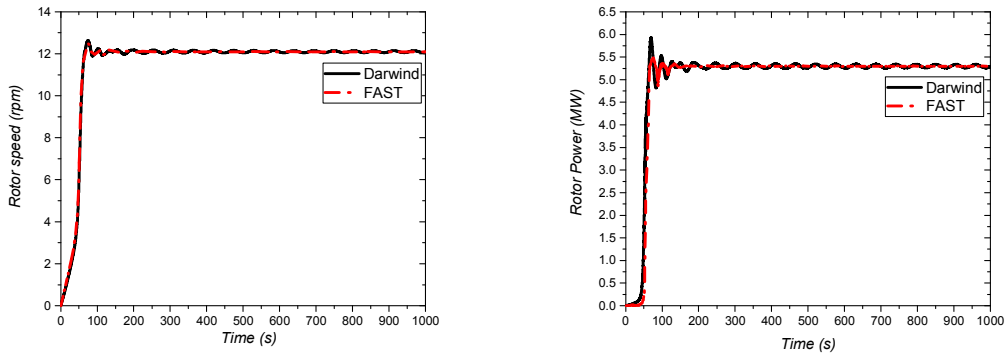

(a) (b)

Fig. 19. Power spectral density of (a) rotor speed and (b) rotor power.

5. Conclusions

This paper presented the fully coupled aero-hydro-servo-elastic methods developed to simulate

floating offshore wind turbines and then reported a series of verifications. Conclusions are as follows:

1) Kinematics and kinetics: Kane's dynamical method combined with the Cardan angles method, the hybrid coordinate dynamical method, the nonlinear deformations model and the adjacent array method was applied to describe the kinematics and kinetics of FOWTs. Flexible bodies, such as blades and towers, were modeled as Bernoulli-Euler beams and were dispersed using the assumed mode method. Some geometric nonlinearities, e.g., coupling axial displacements caused by the lateral displacements, dynamic stiffening effect, were considered. The verifications indicate that these methods are robust and feasible.
2) Aerodynamics: the BEM method with aerodynamic corrections was implemented in the code. In general, tests indicated that the aerodynamic methods are feasible. Nonetheless, compared with the experimental results, the BEM method may not have been sufficiently accurate when the platform moved acutely in a harsh sea states. Hence, the development of more advanced aerodynamic methods is suggested, for example, the free-wake vortex method and the computational fluid dynamics method.
3) Hydrodynamics: a combination of the linear potential-flow theory, the second-order wave force theory, the Morison formula with the strip theory and the additional hydrodynamic damping correction were used in the code. Code-to-experiment comparisons indicated that hydrodynamic loads predicted by the code were reasonable.
4) Mooring system modelling: a quasi-static approach for a catenary mooring system was developed. Code-to-experiment comparisons indicated that the average tensile forces in the code were in good agreement with those measured in the experiment. Nonetheless, the fluctuation of the results predicted by the code was much less than those measured in the experiment. Therefore, the development of dynamic mooring methods in the future is suggested, e.g., the lumped mass method, the spectral method and the finite element method.
5) Control strategies: a generator-torque controller and a blade-pitch controller are used in the code. The comparisons showed there was a great challenge to control all the targets perfectly in practice. We suggest to develop more advanced controllers in the future, such as the individual pitch controller, the tuned mass damper controller, the neural network controller and so on.

In summary, the developed code DARwind which based on coupled aero-hydro-servo-elastic methods could perform fully coupled simulations for FOWTs, and its feasibility was verified by a series of code-to-code and code-to-experiment comparisons. Nonetheless, some improvements should be taken in the future, such as developing a more accurate aerodynamic model, developing more advanced control strategies, and speeding up the code further.

References

[1] T. Xu, Statistics on global wind power installed capacity in 2015, Wind Energy Ind. 5156.2 (2016).

[2] A.J. Coulling, A.J. Goupee, A.N. Robertson, J. Jonkman, H.J. Dagher, Validation of a FAST semi-type floating wind turbine numerical model with DeepCwind test data, J. RENEW. SUSTAIN ENER. 5.2, 023116 (2013).

[3] W. Musial, S. Butterfield, A. Boone, Feasibility of floating platform systems for wind turbines, Proceedings of the 23rd ASME Wind Energy Symposium, Reno, NV (2004).

[4] B. Skaare, T.D. Hanson, R. Yttervik, F.G. Nielsen, Dynamic Response and Control of the Hywind Demo Floating Wind Turbine, Proceedings of Eur. Wind Energy Conf., Warsaw, Poland (2011).

[5] A. Aubault, C. Cermelli, A. Lahijanian, A. Lum, A. Peiffer, D. Roddier, WindFloat Contraption:

From Conception to Reproduction, Proceedings of the 31st International Conference on Offshore Mechanics and Arctic Engineering, Rio de Janeiro, Brazil (2012).
[6] Fukushima Offshore Wind Consortium, Fukushima Floating Offshore Wind Farm Demonstration Project (Fukushima FORWARD), Japan: Fukushima Offshore Wind Consortium (2014) 1–8.
[7] A.M. Viselli, A.J. Goupee, H.J. Dagher, C.K. Allen, VolturnUS 1:8: Conclusion of 18-Months of Operation of the First Grid-Connected Floating Wind Turbine Prototype in the Americas, Proceedings of the 34th International Conference on Ocean, Offshore and Arctic Engineering (2015).
[8] F.G. Nielsen, T.D. Hanson, INTEGRATED DYNAMIC ANALYSIS OF FLOATING OFFSHORE WIND TURBINES, Proceedings of the 25th Int. Conf. Offshore Mech. Arct. Eng., Hamburg, Germany (2006) 1–9.
[9] B.J. Koo, A.J. Goupee, R.W. Kimball, K.F. Lambrakos, Model Tests for a Floating Wind Turbine on Three Different Floaters, J. Offshore Mech. Arct. Eng. 136 (2014) 021904.
[10] F. Duan, Z. Hu, G. Liu, J. Wang, Experimental comparisons of dynamic properties of floating wind turbine systems based on two different rotor concepts, Appl. Ocean Res. 58(2016) 266–280.
[11] F. Duan, Z. Hu, J.M. Niedzwecki, Model test investigation of a spar floating wind turbine, Mar. Struct. 49 (2016) 76–96.
[12] M.J. Muliawan, M. Karimirad, Z. Gao, T. Moan, Extreme responses of a combined spar-type floating wind turbine and floating wave energy converter (STC) system with survival modes, Ocean Eng. 65 (2013) 71–82.
[13] Y. Liu, S. Li, Q. Yi, D. Chen, Developments in semi-submersible floating foundations supporting wind turbines: A comprehensive review, RENEW. SUST. ENERG. REV. 60 (2016) 433-449.
[14] K.H. Lee, Responses of Floating Wind Turbines to Wind and Wave Excitation, M.S. Dissertation (2005) Department of Ocean Engineering, Massachusetts Institute of Technology, Cambridge, MA, USA.
[15] E.N. Wayman, P.D. Sclavounos, S. Butterfield, J. Jonkman, W. Musial, Coupled Dynamic Modeling of Floating Wind Turbine Systems, Proceedings of Offshore Technology Conference, Houston, TX (2006).
[16] M. Karimirad, T. Moan, Extreme dynamic structural response analysis of catenary moored spar wind turbine in harsh environmental conditions, J. OFFSHORE MECH. ARCT, 133.4 (2011) 041103.
[17] E.E. Bachynski, M. Etemaddar, M.I. Kvittem, C. Luan, T. Moan, Dynamic analysis of floating wind turbines during pitch actuator fault, grid loss, and shutdown, Energy Proc. 35 (2013) 210-222.
[18] J.E. Withee, Fully coupled dynamic analysis of a floating wind turbine system, massachusetts inst. of tech. cambridge (2004).
[19] D. Matha, A. Cordle, R. Pereira, J. Jonkman, M. Schlipf, J. Lucas, Challenges in Simulation of Aerodynamics, Hydrodynamics and Mooring-Line Dynamics of Floating Offshore Wind Turbines, Proceedings of the 21th International Ocean and Polar Engineering Conference, Maui, Hawaii (2011).
[20] R.E. Wilson, S.N. Walker, P. Heh, Technical and User's Manual for the FAST_AD Advanced Dynamics Code. OSU/NREL Report (1999) 99-01.
[21] J. Jonkman, L. Marshall, J.R. Buhl, FAST User's Guide-Updated August 2005. No. NREL / TP-500-38230, National Renewable Energy Laboratory (NREL), Golden, CO. (2005).
[22] I. Fylling, K. Mo, K. Merz, N. Luxcey, Floating wind turbine-Response analysis with rigid-body model, Proceedings of European Offshore Wind, Stockholm, Sweden (2009).
[23] W. Zhao, D. Wan, Wind turbine impacts on its semi-submersible floating supporting system for phase II of OC4. Proceedings of the 24th International Ocean and Polar Engineering Conference,

Busan, South Korea (2014).
[24] Y. Liu, P. Yao, D. Wan, Numerical investigation on interaction between a semi-submersible platform and its mooring system, Proceedings of the 34th International Conference on Ocean, Offshore and Arctic Engineering, St John's, NL, Canada (2015).
[25] A. Nematbakhsh, E.E. Bachynski, Z. Gao, T. Moan, Comparison of wave load effects on a TLP wind turbine by using computational fluid dynamics and potential flow theory approaches, APPL. OCEAN RES. 53 (2015) 142-154.
[26] J. Jonkman, W. Musial, Offshore code comparison collaboration (OC3) for IEA task 23 offshore wind technology and deployment. Contract 303 (2010) 275–3000.
[27] A. Robertson, J. Jonkman, W. Musial, F. Vorpahl, W. Popko, Offshore Code Comparison Collaboration, Continuation : Phase II Results of a Floating Semisubmersible Wind System, Proceedings of EWEA Offshore conference (2013) 1–15.
[28] T.R. Kane, D.A. Levinson, The Use of Kane's dynamical Equations in Robotics, Int. J. Rob. Res. 2 (1983) 3–21.
[29] S.J. Tupling, M.R. Pierrynowski, Use of cardan angles to locate rigid bodies in three-dimensional space, MED. BIOL. ENG. & COMPUT. 25.5 (1987) 527-532.
[30] P.W. Likins, Finite element appendage equations for hybrid coordinate dynamic analysis, Int. J. Solids Struct. 8 (1972) 709–31.
[31] R.L. Huston, W.K. James, A discussion on constraint equations in multibody dynamics, Mechanics Research Communications, 9 (1982) 251-256.
[32] H. Glauert, Airplane Propellers, Aerodyn Theory, (1935) 169–360.
[33] M.O.L. Hansen, Aerodynamics of wind turbines, Routledge, 2015.
[34] O. Faltinsen, Sea loads on ships and offshore structures, Cambridge university press, 1993.
[35] M. Masciola, J. Jonkman, A. Robertson, Implementation of a multisegmented, quasi-static cable model, Proceedings of the 23th International Offshore and Polar Engineering Conference. International Society of Offshore and Polar Engineers, Alaska, USA (2013).
[36] J. Jonkman, Dynamics of offshore floating wind turbines—model development and verification, Wind energy 12.5 (2009) 459-492.
[37] R.C. Alperin, The matrix of a rotation. College Math. J. 20.3 (1989) 230-230.
[38] A.A. Nada, B.A. Hussein, S.M. Megahed, A.A. Shabana, Use of the floating frame of reference formulation in large deformation analysis: experimental and numerical validation. Proceedings of Inst. Mech. Eng. Part K. J. Multi-Body Dyn. 224 (2009) 45–58.
[39] N.F. Morris, The use of modal superposition in nonlinear dynamics, Computers & Structures, 7.1 (1977) 65-72.
[40] J.Y. Liu, J.Z. Hong, Dynamics of three-dimensional beams undergoing large overall motion. Eur. J. Mech. A/Solids, 23 (2004) 1051–68.
[41] J. Chen, Z. Hu, A higher-order coupling model of the blades of the floating offshore wind turbine. Proceedings of the 6th International Conference on Marine Structures-MARSTRUCT, Lisbon, Portugal. 877-888 (2017).
[42] S. Øye, FLEX4 simulation of wind turbine dynamics, Proceedings of the 28th IEA Meeting of Experts Concerning State of the Art of Aeroelastic Codes for Wind Turbine Calculations (1996).
[43] W.J. Rankine, On the mechanical principles of the action of propellers, Transactions of the Institution of Naval Architects 6 (1865).
[44] R.E. Froude, On the part played in propulsion by difference of fluid pressure. Transactions of the

Royal Institution of Naval Architects, 30 (1889) 390-405.
[45] D.A. Spera, Wind Turbine Technology, ASME Press, New York, 1994.
[46] J.G. Schepers, H. Snel, Dynamic Inflow: Yawed Conditions and Partial Span Pitch Control, ECN-C- -95-056, Petten, The Netherlands, 1995.
[47] S. Øye, Dynamic stall, simulated as a time lag of separation, Proceedings of the 4th IEA Symposium on the Aerodynamics of Wind Turbines, Harwell Laboratory, Harwell, UK (1991).
[48] B.J. Jonkman, TurbSim user's guide: Version 1.50, 2009.
[49] J.N. Newman, Marine Hydrodynamics. The MIT Press: Cambridge, MA, 1997.
[50] C.H. Lee, WAMIT theory manual. Massachusetts Institute of Technology, Department of Ocean Engineering, 1995.
[51] J. M. Jonkman, A. Robertson, G. J. Hayman. HydroDyn user's guide and theory manual. *National Renewable Energy Laboratory* (2014).
[52] C.H. Lee, J.N. Newman. The computation of second-order wave loads. 1991.
[53] J.N. Newman, Second-order, slowly-varying forces on vessels in irregular waves, 1974.
[54] Y. Ma, Z. Hu, L. XIAO, Wind-wave induced dynamic response analysis for motions and mooring loads of a spar-type offshore floating wind turbine, Journal of Hydrodynamics, Ser. B 26.6 (2015) 865-874.
[55] J.M. Jonkman, Dynamic modeling and load analysis of an offshore floating wind turbine, Ph.D. Thesis (2007), Department of Aerospace Engineering Sciences, University of Colorado, Boulder, CO.
[56] J. Jonkman, S. Butterfield, W. Musial, G. Scott, Definition of a 5-MW reference wind turbine for offshore system development. National Renewable Energy Laboratory, Golden, CO, Technical Report (2009), No. NREL/TP-500-38060.
[57] A. Robertson, J. Jonkman, M. Masciola, H. Song, A. Goupee, A. Coulling, C. Luan, Definition of the semisubmersible floating system for phase II of OC4, Offshore Code Comparison Collaboration Continuation (OC4) for IEA Task 30 (2012).
[58] J. Chen, Z. Hu, Experimental investigation of aerodynamic effect–induced dynamic characteristics of an OC4 semi-submersible floating wind turbine, Proceedings of the Institution of Mechanical Engineers, Part M: Journal of Engineering for the Maritime Environment (2017) 1475090217706194.
[59] J. Chen, Z. Hu, D. Wan, Q. Xiao. Comparisons of the dynamical characteristics of a semi-submersible floating offshore wind turbine based on two different blade concepts. Ocean Engineering, 153, 305-318 (2018).
[60] Z. Hu, J. Chen, G. Liu, Investigation on High-order coupled rigid-flexible multi-body dynamic code for offshore floating wind turbines, Proceedings of the 36th Int. Conf. Ocean, Offshore Arct. Eng., Trondheim, Norway (2017).
[61] B. Boukhezzar, L. Lupu, H. Siguerdidjane, M. Hand, Multivariable control strategy for variable speed, variable pitch wind turbines, RENEW. ENERG. 32.8 (2007)1273-1287.